Precision Engineering 60 (2019) 167–177

Contents lists available at ScienceDirect

Precision Engineering

journal homepage: www.elsevier.com/locate/precision

Experimental validation of complex non-minimum phase zeros in a flexure mechanism

Leqing Cui*, Shorya Awtar

Precision Systems Design Lab, Mechanical Engineering, University of Michigan, Ann Arbor, MI, 48109, USA

ABSTRACT

In this paper, we present the design of an experimental setup that validates the existence of complex non-minimum phase (CNMP) zeros in a flexure mechanism under specific conditions. Using this setup, the dynamics of a lightly damped, nominally symmetric XY flexure mechanism comprising two double parallelogram flexure modules (DPFM) is experimentally studied while varying the operating point and parametric asymmetry. While CNMP zeros have been reported in analytical studies, a direct experimental validation of model-based prediction poses several challenges and is rare in the literature. The challenges addressed in the presented experimental setup design include isolating the specific dynamics of interest while minimizing extraneous dynamics, avoiding friction and backlash in the system to offer clean and repeatable measurements, and employing simple and practical sensing and actuation methods. This experimental setup is used to obtain X direction frequency response measurements and thereby record the presence or absence of CNMP zeros, while varying the Y direction operating point and the mass asymmetry between two DPFMs. This experimental evidence of the existence of CNMP zeros under specific conditions agrees well with the previous model-based predictions.

1. Introduction and motivation

The objective of this paper is to provide an experimental validation of the intriguing phenomenon of complex non-minimum phase (CNMP) zeros previously modelled and predicted for a certain XY flexure mechanism [1,2]. Flexure mechanisms are commonly used as the bearing stage in high-precision motion systems [3,4]. For a given choice of sensor and actuator location in these motion systems, the input-output transfer function is used as the basis for control system design to achieve desired motion specifications such as speed of response or bandwidth, disturbance and noise rejection, stability over range of operation, etc.

Recent results in the dynamic modeling of flexible systems have shown that CNMP zeros can appear in the input-output transfer function of such a system if it has at least one lower frequency mode followed by two closely-spaced modes [1]. This was demonstrated using the example of a certain representative XY flexure mechanism model that employs two double parallelogram flexure modules (DPFM) as building-blocks in a symmetric layout, which is shown in Fig. 1. The vibration of the two secondary stages associated with two DPFM in this case gives rise to two closely spaced modes. This particular XY flexure mechanism model was employed simply as a means to systematically investigate – theoretically in previous work [2] and experimentally in this work – the phenomenon of CNMP zeros under varying conditions. This XY flexure mechanism model was not intended to serve as the bearing stage of a practical motion system for any given application. The derived theoretical dynamic model for this mechanism demonstrated that CNMP zeros can indeed arise in the X direction input-output transfer function for predictable combinations of Y operating point and mass parameter asymmetry between the two secondary stages [2].

This appearance of CNMP zeros (i.e. a complex conjugate pair on the right-hand side of the s-plane) is important to investigate because such zeros are rare in flexible mechanical systems and are highly detrimental to control system performance [5–9]. Non-minimum phase (NMP) zeros, including the particular case of CNMP zeros, impose a tradeoff between close-loop bandwidth (which impacts speed of response), stability robustness, and disturbance rejection (which impacts position resolution) [1]. Typically, zeros in flexible mechanical systems are complex conjugate pairs lying slightly to the left of the imaginary axis in the s-plane, i.e. complex minimum phase (CMP), or on the real axis of the s-plane (i.e. real minimum or non-minimum phase) [10–12]. The above-mentioned modeling work not only shows the existence of CNMP zeros, but even more importantly predicts the specific parametric values (i.e. physical system design choices) for which these CNMP zeros appear or can be eliminated over the entire operating range of interest. While these theoretical findings are significant from the perspective of physical design, dynamics and control of a flexure-based motion system, in particular, and broadly relevant to flexible systems in general, there remains a need to experimentally validate these theoretical predictions, which is the primary focus of this paper.

From a design perspective, there are several factors that can

---

* Corresponding author.
E-mail addresses: leqing@umich.edu (L. Cui), awtar@umich.edu (S. Awtar).

https://doi.org/10.1016/j.precisioneng.2019.08.002
Received 1 July 2018; Received in revised form 23 July 2019; Accepted 9 August 2019

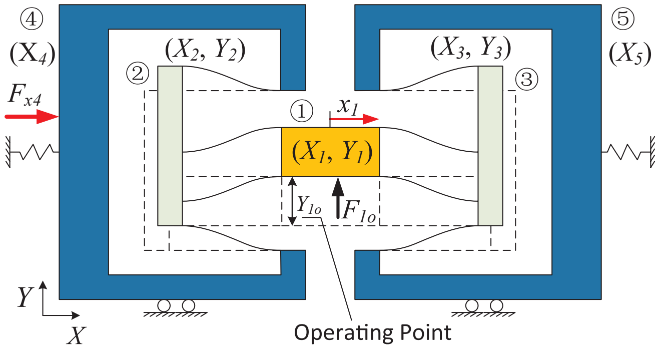

Fig. 1. XY flexure mechanism model.

influence the existence of CNMP zeros in a flexure mechanism based motion system. For example, a co-located sensor and actuator arrangement [13] ensures no CNMP zeros, but that generally compromises range of motion or end-point sensing [14]. Alternatively, multiple points of sensing and actuation in any given motion direction can eliminate CNMP zeros, but that decision also entails a consideration of the motion stage size, weight, and cost constraints for a given application [15–17]. A common good design practice is to employ a means to mitigate the under-constraint associated with the secondary stages of the DPFM [18–21]. When employed, this design option pushes out the frequency of the closely spaced modes that can still lead to CNMP zeros under certain conditions. Furthermore, there can be instances of CNMP zeros that arise due to other closely spaced modes of the flexure mechanism, independent of the DPFM secondary stages. The inclusion of adequate and appropriately located damping can also suppress or delay the appearance of such zeros [1,22] but brings its own design challenges.

All these design considerations are available to the mechatronic engineer who carefully weighs various tradeoffs while designing a flexure-based motion system to meet specific motion requirements under various practical constraints. In this paper, our goal is to elucidate a more comprehensive understanding of the system dynamics (specifically CNMP zeros) via experimental validation, which in turn can inform physical system design decisions in a deterministic manner. In particular, this work experimentally confirms that CNMP zero can indeed be eliminated via intentional parameter asymmetry, independent of any of the other design considerations listed above.

2. Background and literature review

In our investigation, CNMP zeros were first encountered in the experimental characterization of an XY flexure mechanism that was intended for large range nanopositioning [23]. This observation led to a theoretical investigation on why and when such zeros arise. This theoretical investigation predicted that a quartet of CMP-CNMP zeros appears in a lightly damped flexible system with one low frequency rigid body mode and two closely spaced modes at a higher frequency if the modal residues[1] of these three modes, when listed in the order of frequency, have alternating signs [1]. This quartet of zeros is symmetric with respect to both the real and imaginary axes on the complex s-plane, with a CMP zero pair to the left of the imaginary axis and a CNMP zero pair to the right of the imaginary axis. To test this theory in the context of flexure mechanisms, we selected a representative XY flexure mechanism model that met the above conditions. This XY flexure mechanism model, shown in Fig. 1, had two closely spaced modes resulting from the symmetric layout of two DPFM as well as a rigid body mode at a lower frequency. Furthermore, this layout allows for investigating the X direction dynamics for different Y operating points. Additionally, even though the layout is nominally symmetric, a small intentional asymmetry was introduced between the masses of the secondary stages of the two DPFM. Thus, this XY flexure mechanism model allowed for the theoretical investigation into the existence of CNMP zeros in the X direction dynamics for different values of Y operating point and mass asymmetry. This investigation demonstrated that for certain predictable combinations of Y operating point and mass asymmetry, the condition of alternating signs of modal residues is met and the NMP-CNMP zero quartet arises. Therefore, this XY flexure mechanism model served as a useful means to investigate CNMP zeros; however, this mechanism was not created to serve the bearing stage in an actual motion system application.

For the theoretical modeling, the non-collocated transfer function from the X direction force (F_{x4}) on stage ④ to the X direction displacement (X_1) of the motion stage (i.e. stage ①) was examined as a function of the Y direction operating point (Y_{1o}) of the motion stage using a lumped-parameter model [2]. This model assumed five masses labeled ① through ⑤ in Fig. 1, with no rotation by design, resulting in ten displacement coordinates in the XY plane. The Y displacements of stages ④ and ⑤ were assumed to be constrained via appropriate bearings (although rollers are schematically shown in Fig. 1, elastic flexures were used in the actual fabricated hardware). It was shown that the geometric non-linearity associated with arc-length conservation in individual flexure beams results in one independent kinematic relation between the relative X and Y displacement coordinates if each parallelogram, resulting in four such kinematic relations [2].

Therefore, the dynamics of the XY flexure mechanism model of Fig. 1 could be modeled via four independent displacement coordinates and resulted in four vibrational modes. The first mode represents a "rigid-body" mode, where all the five stages oscillate with approximately the same magnitude and phase in the X direction. The second mode, denoted as the Y-mode, is associated with the Y-direction oscillation of stages ①, ② and ③. Since the transfer function under study is from the X direction force on stage ④ (F_{x4}) to the X direction displacement of the motion stage (i.e. stage ①), the second mode is unobservable in this transfer function. The third and fourth modes are closely spaced modes and are associated with Y direction oscillations of the secondary stages ② and ③ of the two DPFMs, moving out-of-phase and in-phase, respectively. The modal frequencies and modal residues (magnitude and sign) of these two closely spaced modes were varied by introducing an intentional parametric asymmetry (mass difference between stages ② and ③, given by $\Delta m_{23} = m_2/m_3 - 1$) to simulate unintentional real-life manufacturing tolerances and a potentially intentional design variable. Since, for non-zero Y direction operating points (Y_{1o}) of the motion stage, the above-mentioned kinematic relations for the four parallelograms lead to a coupling between the Y displacement of the secondary stages ② and ③ and the X displacement of the motion stage. As a result, the third mode is observable in the X direction transfer function for non-zero Y operating points irrespective of mass asymmetry while the fourth mode is observable only for non-zero Y operating points and non-zero mass asymmetry.

The first (i.e. rigid-body) mode along with the closely spaced third and fourth modes create the conditions that are necessary for the appearance of CNMP zeros. The ability to vary the operating point (Y_{1o}) and the parametric asymmetry (Δm_{23}) allows for specific predictable combinations of operating point and parametric asymmetry that are sufficient for the appearance of CNMP zeros. There are several noteworthy outcomes of this previous modeling work. First, this model of a simple but representative XY flexure mechanism is able to predict the existence of CNMP zeroes in the X direction transfer function under certain specific conditions. This opens the doors to developing a similar understanding and predictability of CNMP zeros in more complex yet practically useful XY flexure mechanisms [4,24]. Second, the analytically predicted CNMP zero map shows that one can intentionally choose

---

[1] When the input-output transfer function of a system is expressed as a summation of the system's modes (often referred to as modal decomposition), the coefficient of each respective mode is referred to as the *modal residue*.

a certain physical design asymmetry (e.g. $\Delta m_{23} < 0$) to entirely eliminate the CNMP zeros over the entire Y direction operating range, thereby enabling better dynamic performance. This is an important physical system design insight, which is otherwise not obvious. While these previous results and predictions hold considerable promise for dynamic performance, they are based on analytical modeling and numerical simulations that make various assumptions. An experimental validation of this model is of considerable value to corroborate the theoretical understanding gained on the existence of CNMP zeros. Such an experimental validation is the goal of this paper.

A detailed review of the literature on NMP zeros and more specifically CNMP zeros is previously covered in Refs. [1,2]. Tohyama [25] presents CNMP zeros in the context of acoustics of a room but does not cover any experimental measurements. There are only a few existing references that focus on experimental measurements of CNMP zeros. Among these, Loix et al. [26] experimentally confirmed CNMP zeros predicted by numerical modeling for a non-collocated conservative system – a single flexible beam with variable sensor location. Awtar [27] predicted and experimentally corroborated CNMP zeros in the non-collocated transfer function of a multi-spring multi-mass servo system. These CNMP zeroes arose as a result of electromagnetic coupling between the DC motor and tachometer in the servo system. For flexure mechanisms, experimental validation of CNMP zeros under varying conditions (operating point and parametric asymmetry) has not been reported in the prior literature to the best of our knowledge. Such an experimental validation poses unique challenges in the experimental hardware setup design and obtaining reliable measurements, as listed below:

1. An experimental validation requires that we create a hardware setup that captures the XY flexure mechanism model of Fig. 1 and its inherent assumptions to produce the dynamics of interest, specifically the lower frequency rigid-body mode (first mode in the model) and two closely spaced modes (third and fourth modes in the model), all of which are in-plane (XY) modes. In reality, there will always be additional in-plane modes (e.g. rotational), out-of-plane modes, distortion modes due to the compliance of the “supposedly rigid” stages of the flexure mechanism, and modes associated with individual flexure beam dynamics. Therefore, the hardware setup has to be designed such that any such extraneous modes occur at *much higher* frequencies (quantified in Section 2.1) than the modes of interest (modes 1, 3 and 4 modeled above). This is to ensure that these extraneous modes have a negligible impact in the frequency range of the modes of interest.
2. As noted above, the CNMP zeros in the simple representative XY flexure mechanism model are the result of interaction between the two closely spaced modes, and a small but finite contribution from the lower frequency “rigid-body” mode. Therefore, the hardware setup has to be designed to have two closely spaced modes that are *well-separated* (quantified in Section 2.1) from the “rigid-body” mode modeled above as well as any other extraneous “rigid-body” modes at lower frequencies.
3. This experimental validation requires the detection of CNMP zeros in the X direction frequency response function at various Y direction operating points. The X direction bearing, sensor, and actuator should be designed or selected to avoid non-linearities such as friction and backlash so as to enable high resolution, repeatable and reliable frequency response function measurements.
4. The actuation method to establish the Y direction operating point has to be such that it can provide a constant, purely Y direction force that is free of friction and backlash. Also, the implementation of this Y direction actuation should not impose any X direction constraints on the motion stage so as to avoid altering the X direction system dynamics under investigation. Finally, this Y direction actuation should be capable of providing varying levels of Y direction force to produce varying Y operating points in a simple and practical manner.

In this paper, we present an experimental hardware setup and associated measurements that addresses all of the above challenges via several careful design considerations. The sources of extraneous dynamics are either eliminated or adequately separated from the dynamics of interest via appropriate structural design. Simple sensing and actuation methods are selected to ensure reliability and repeatability in measurement. The primary contribution of this work is a first-of-its-kind experimental validation of CNMP zeros that have been previously predicted under specific varying conditions by a theoretical model. This experimental validation helps confirm that the geometric arc length conservation in flexure beams indeed leads to coupling between motions in the X and Y directions. By validating the outcomes of the previous theoretical model, the experimental results of this paper support the various modeling assumptions made, thereby justifying the use of similar assumptions in future modeling efforts for other flexure mechanisms. Most importantly, these experimental results help equip the mechatronic engineer with the knowledge that CNMP zeros can not only be predicted but also eliminated via simple physical design choices such as intentional parametric asymmetry.

Even though the CNMP zeros experimentally investigated here arise due to the closely spaces modes associated with the Y displacement of the secondary stages of the two DPFM, such zeros can more generally arise from any two closely spaced modes in a flexure mechanism. The experimental hardware setup design and measurement methods presented in this paper are equally relevant and applicable to any such scenario.

The rest of this paper is organized as follows. Section 3 covers the detailed procedure of designing the experimental setup including the evolution of the flexure mechanism geometry and the selection and optimization of overall dimensions to achieve the desired dynamics (mode shapes and frequencies). Section 4 describes the fabrication and assembly of experimental set-up including selection and integration of sensing and actuation methods. Section 5 presents the operation of the experimental setup and the resulting measurements. These measurements are compared with the model-based predictions, followed by a discussion on the observations. Section 6 summarizes the key conclusions and plans for future work.

3. Experimental setup: flexure mechanism geometry design

The goal here is to design an experimental setup that captures the dynamics of interest of the simple representative XY flexure mechanism (Fig. 1) in a systematic, step-by-step manner, specifically the two closely spaced modes (CSM) associated with Y direction oscillations of the secondary stages ② and ③ and the lower frequency “rigid-body” mode where all of the five stages oscillate in phase in the X direction. At the same time, it is desirable that any other modes (referred to as extraneous modes in this paper), which are to be expected in a physical experimental set-up, remain “well-separated” from the modes of interest. Following conventional practice, we define “well-separated” as one decade of separation in the frequency domain. Specifically, we consider a high frequency extraneous mode (ω_h) to be well-separated w.r.t. the closely spaced modes (ω_u and ω_v, with $\omega_v > \omega_u$) when the frequency separation of the former from the latter is more than 10 times the frequency separation between the two CSM. Mathematically, this may be stated as:

$$SEP_h = \frac{\omega_h/\omega_o - 1}{\omega_v/\omega_u - 1} > 10 \tag{1}$$

where

$$\omega_o \triangleq \sqrt{\omega_u \omega_v} \tag{2}$$

By definition, ω_o represents the mid-point of ω_u and ω_v on a log scale. Similarly, we want to make sure that the lower frequency rigid body mode (ω_l) is also well-separated from the CSM, and a similar mathematical definition may be used:

$$SEP_l = \frac{\omega_o/\omega_l - 1}{\omega_v/\omega_u - 1} > 10 \tag{3}$$

while we used the above definition of "well-separated" for the purpose of designing our experimental set-up, in general "well-separated" is a relative concept. Therefore, one can equally well use a slightly different definition. Also, over the entire range of operating points and parametric asymmetry studied here, the closely spaced modes (ω_u and ω_v) shift by small amounts. Given that these shifts are small, we only assumed the nominal conditions (i.e. zero operating point and zero asymmetry) in the experimental setup design phase when considering SEP_h and SEP_l. Furthermore, these separation indices are solely based on the natural frequencies, which provide an initial guideline in the early design phase. At a later phase in the design, we also consider the contribution of a given mode, which depends on the sensor location. For example, if a mode is unobservable at the sensor location, it has a minor contribution at frequencies around ω_O, even if it does not satisfy the above separation requirements.

As the first step in the design process, we replaced the roller bearings shown in Fig. 1 with flexure bearings to eliminate friction and backlash in the experimental setup. This also enables the setup to be manufactured monolithically from a single flat metal plate, thereby minimizing assembly and providing a common ground reference for other components. An initial design iteration shown in Fig. 2a utilizes four simple *beam flexures* to provide X direction bearing for stages ④ and ⑤. A *balan*ce mass with the same mass value of the mover of the actuator (discussed in Section 4.2) is added on the opposite side of the actuator to achieve the same mass (nominally) for stages ④ and ⑤. The reason to pursue this nominally balanced mass is to align the Center of Stiffness in the out-of-plane (Z) direction with the Center of Mass. This helps increase the frequency of any "rigid-body" rotational modes about the Y axis. But the drawback of the simple beam flexures as arranged in Fig. 2a is the limited travel range in the X direction due to geometric over-constraint. To relieve this over-constraint, the simple beam flexures were replaced by *folded beam flexures* as shown in Fig. 2b.

As the initial choice of dimensions for the main DPFMs in Fig. 2, we used typical dimensions from a previous XY flexure mechanism design [4]. Accordingly, the length of the DPFM's beams (L_1 in Fig. 2b) was set at 47.5 mm and thickness (T_1) was set at 0.625 mm. The length of the folded beam flexures (L_F in Fig. 2b) was set at 40 mm and the thickness was set at 0.625 mm. Based on these beam dimensions, the masses of the various moving stages were initially selected to be $m_1 = 0.2$ kg, $m_2 = m_3 = 0.04$ kg, and $m_4 = m_5 = 0.8$ kg. These mass values were simply a starting point and were subsequently iterated during the modal analysis described below. An additional consideration in selecting these various dimensions and masses was to achieve a practically viable desktop size experimental setup.

A modal analysis was conducted on the design of Fig. 2b using linear finite elements analysis (FEA), with stage ① at the nominal operating position (i.e., $Y_{1o} = 0$). Even though previous non-linear analysis has shown that the natural frequencies of the two CSM vary slightly with the operating point [2], this variation is small enough for purpose of the experimental setup design, where the primary goal is to achieve adequate separation between the modes of interest and extraneous modes. For the modal analysis FEA, tetrahedron solid elements were used. Adaptive mesh sizing was employed with smaller size elements for the beams and larger size for the stages.

The results of the modal analysis of the experimental set-up designs (iterations Fig. 2b thorough Fig. 2d) are compiled in Table 1. The unshaded modes are those that correspond to the four modes of the XY flexure mechanism of Fig. 1 and are therefore the modes of interest. The

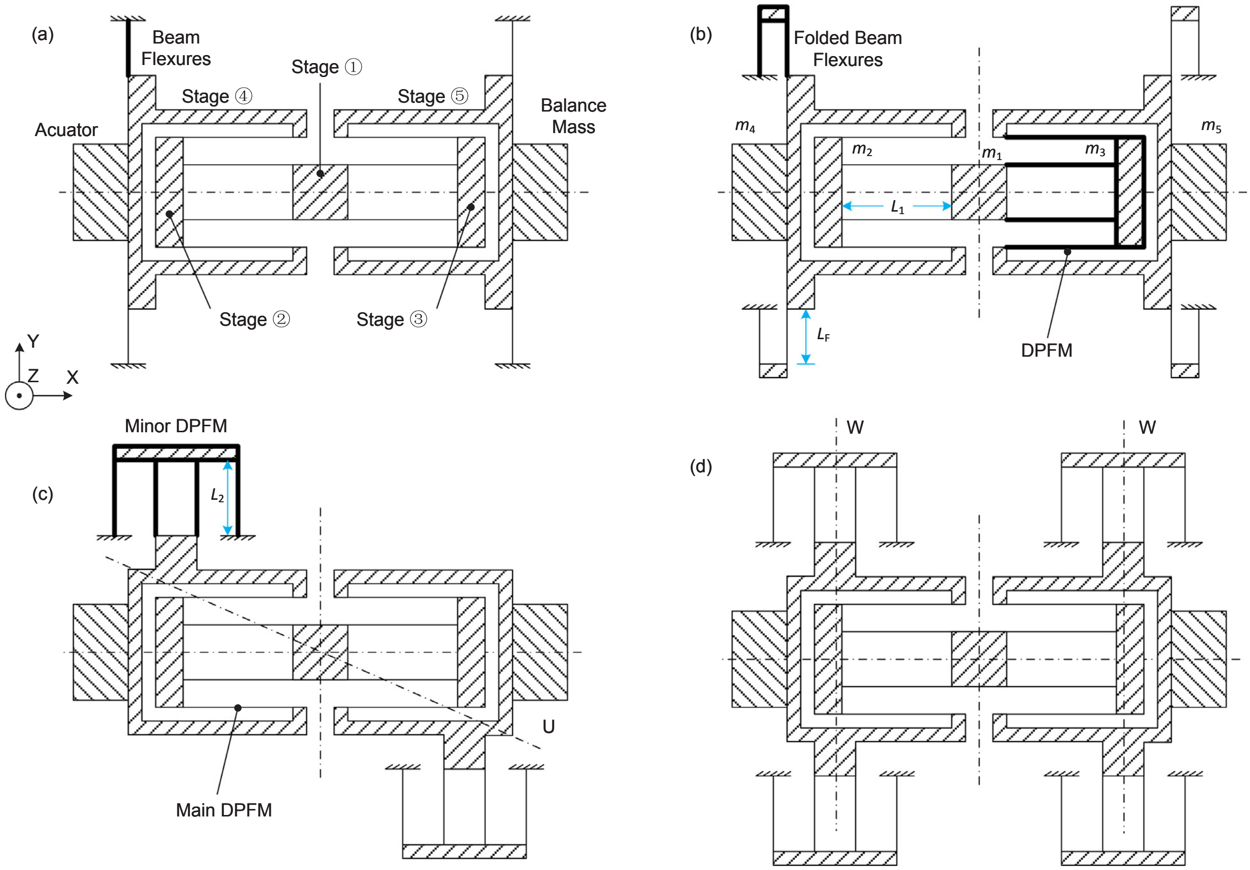

Fig. 2. Geometric evolution of the experimental setup design.

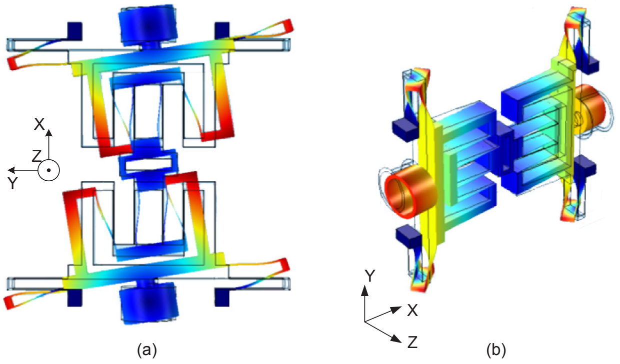

Fig. 3. Examples of extraneous modes in Fig. 2b: (a) III mode; (b) VII mode.

remaining modes (shaded) of the experimental setup design are extraneous modes, which are not of interest in the current investigation. For the design of Fig. 2b, the first two modes are modes of interest. However, there are several extraneous modes (III through VI) before the next modes of interest (CSM1 and CSM2) appear. For example, mode III is an in-plane rotational mode as shown in Fig. 3a, while the mode VII is an out-of-plane rotational mode as shown in Fig. 3b. The associated separation indices are lower than desired: $SEP_l = 5.2$ and $SEP_h = 5.8$.The reason for these multiple rotational modes appearing at low frequencies is that the folded beam flexure has inadequate stiffness in its bearing directions (e.g. Y translation, Z translation, Y rotation, Z rotation, etc.) [28].

To improve the stiffness in these bearing directions, the folded beam flexures in Fig. 2b are replaced with DPFMs as shown in Fig. 2c. DPFM offer better stiffness characteristics without sacrificing the travel range [28,29]. These additional DPFMs are denoted as "minor" DPFMs to distinguish from the two previous DPFMs (denoted as the "main" DPFMs). The beams of the minor DPFMs were initially designed with the same dimensions as the beams in the main DPFM, with length (L_2) set as 47.5 mm and thickness (T_2) set as 0.625 mm. Furthermore, to reduce the frequencies of the two CSM and achieve desired SEP_h, m_1 was increased from 0.2 kg to 0.4 kg, and m_2 and m_3 were increased from 0.04 kg to 0.06 kg.

The modal analysis results for Fig. 2c design show that the number of extraneous modes between the modes of interest has reduced. However, since the geometry of Fig. 2c is not symmetric w.r.t to both the X and Y axes, the flexure mechanism has an axis connecting the grounds (denoted by U-axis in Fig. 2c) with low rotational stiffness. In fact, the extraneous out-of-plane modes III and IV are associated with the rotation about the U-axis. The separation indices for this design are $SEP_l = 6.2$ and $SEP_h = 2.6$, which are still inadequate.

A logical improvement to Fig. 2c was to employ four minor DPFMs to achieve symmetry w.r.t. both the X and Y axes. This resulted in the design shown in Fig. 2d. The modal analysis results (Table 1) for this design show that the rotational modes about the U-axis in Fig. 2c are effectively eliminated. Moreover, all of the first four modes are also the modes of interest, with separation indices of $SEP_l = 19.3$ and $SEP_h = 4.2$. It is clear that the latter needs to be further increased. Moreover, the four closely spaced modes (from VII to X) are associated with the oscillation of the secondary stages in the four minor DPFMs. These extraneous closely spaced modes also need to be moved to higher frequencies.

Modes V and VI of Fig. 2d design are shown in Fig. 4a and Fig. 4b, respectively. For both these modes, stage ① is almost stationary, thus separating the flexure mechanism symmetrically into two sides w.r.t. stage ①. Furthermore, each side rotates about a W-axis (parallel to the Y direction), which represents the location where two minor DPFMs connect to a main DPFM (see Figs. 2d, 4a and 4d). The frequencies of these two modes are mainly determined by the dimensionsL_3, L_4, and L_5 (shown in Fig. 4d) as discussed next.

L_3 is the span of the inner parallelogram of the minor DPFM, which affects the rotational stiffness about the W-axis. When L_3 is small, the rotational stiffness is dominated by the torsion stiffness of the individual beams. However, when L_3 is increased, the rotational stiffness is driven by the Z direction stiffness of the individual beams and the span (L_3) of the inner parallelogram. With the typical dimensions used in this study (e.g., $T_2 = 0.625$ mm, out-of-plane height$H_2 = 25.4$ mm, $L_2 = 47.5$ mm, and $L_3 = 20$ mm), the torsional stiffness of a single beam about W-axis is 1.099 (N m/rad) at the tip [30]; in comparison, the contribution to rotational stiffness by an individual beam due to its Z direction stiffness along with a lever arm of 10 mm (i.e., half of L_3) is 3.714 (N m/rad). Therefore, since increasing L_3 helps increase the torsional stiffness of the minor DPFM about the W-axis, it was increased from 20 mm to 40 mm. But this also leads to a larger size (and therefore heavier) secondary stage of the minor DPFM, which can reduce the natural frequencies of the modes associated with the secondary stages of the minor DPFMs. The selection of dimensions of the secondary stage of the minor DPFM (i.e., L_6 and L_7) is discussed later in this section.

L_4 and L_5 affect the rotational inertia associated with the rotational modes V and VI. The design objective is to minimize the mass of stage ④ and have its center of mass center lie close to the W-axis such that one can minimize the rotational inertia about the W-axis, thus increasing the natural frequencies of the corresponding rotational modes. Given other considerations of geometric layout, we chose $L_4 = 85$ mm and $L_5 = 30$ mm to be as small as possible.

Mode VII of Fig. 2d design is shown in Fig. 4c as an example of the four closely spaced modes associated with the secondary stages of the minor DPFMs. To increase the natural frequencies of these modes, one can either increase the X direction stiffness of the minor beams (i.e. reduce length L_2 and/or increase thickness T_2) or lower the mass of the minor secondary stages (i.e. reduce dimensions L_6 and L_7). However, there are tradeoffs in all these choices.

Increasing the X direction stiffness X direction of the minor DPFM also increases the frequency of the "rigid-body" mode (i.e., mode I of Fig. 2d design listed in Table 1) bringing it closer to the two CSM and adversely impacting the SEP_l index. This tradeoff was carefully balanced to create adequate frequency separation between the two CSM and the "rigid-body" mode, as well as between the two CSM and the higher frequency extraneous modes related to the secondary stages of the minor DPFMs (e.g. mode VII of Fig. 2d design). By iteratively selecting dimensions and checking the mode shapes and frequencies, we chose $L_2 = 47.5$ mm and$T_2 = 1$ mm.

Reducing L_7 results in a smaller span of the outer parallelogram of the minor DPFM, thus lowering the rotational stiffness about the W-axis and the natural frequencies of modes V and VI. The rotational stiffness about the W-axis has a quadratic dependence on the inner span L_3 as well as the outer span L_7. We chose $L_7 = 80$ mm, which is twice the inner span L_3, to ensure an adequately high rotational stiffness about the W-axis to keep modes V and VI well-separate from the two CSM.

Reducing L_6 increases the in-plane bending compliance of the minor DPFM secondary stages resulting in a lower translational stiffness of the minor DPFM along the Y direction which can introduce additional extraneous in-plane modes associated with the Y translation or Z rotation of stages④ and ⑤. One way to overcome the tradeoff between the mass and stiffness of the minor secondary stages is to use a truss-like or honey-comb structure. However, this proved to be unnecessary for the present study. By simply iterating upon the dimensions, we were able to achieve adequately high natural frequency of the minor stages in the X direction (e.g. mode VII) as well as adequately high Y direction stiffness of the minor DPFMs to avoid any extraneous in-plane modes at low frequencies. In the final iteration, we chose $L_6 = 3$ mm.

The final set of dimensions for Fig. 2d (Improved) design is listed in Table 2. The modal analysis results for this design are listed in Table 1 alongside the results for Fig. 2d design with the initial set of dimensions. As seen in this table, the separation indices for Fig. 2d (Improved) design are $SEP_l = 19.8$ and $SEP_h = 24.5$, which indicates a satisfactory

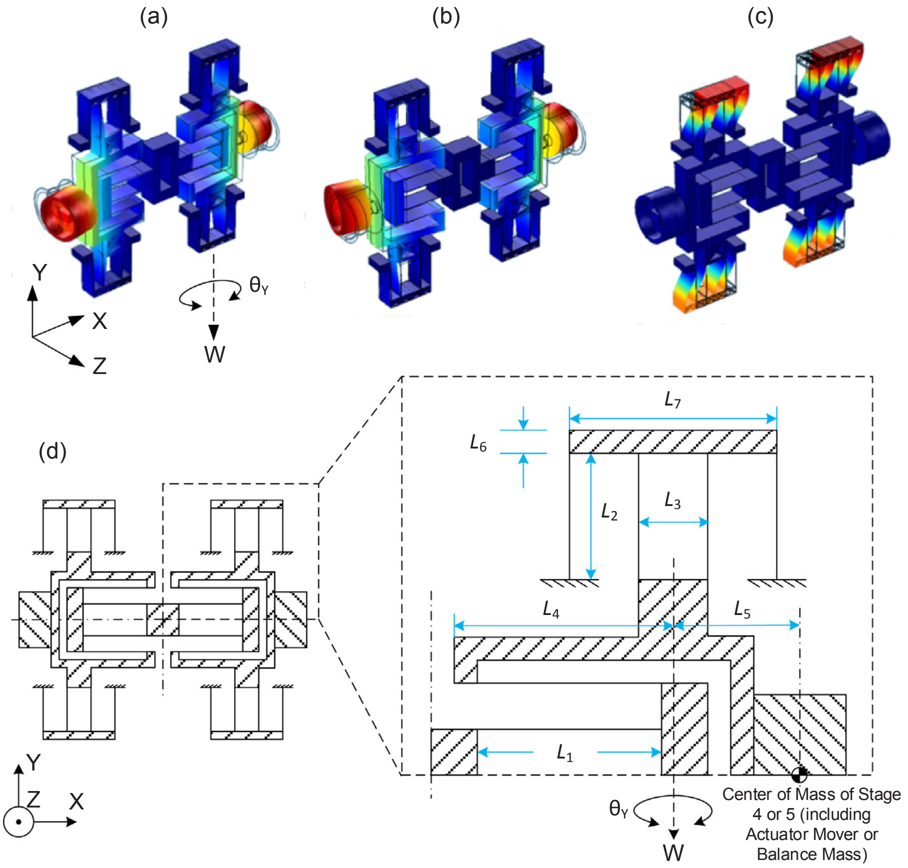

Fig. 4. Extraneous modes of Fig. 2ddesign: (a) mode V, (b) mode VI, (c) mode VII, and (d) relevant dimensions of Fig. 2d design.

frequency separation. The first eight modes of this design are shown in Fig. 5, and several observations are noted below.

1. The rigid-body mode now appears as mode II due to increase in the X direction stiffness of the minor DPFMs. However, since mode I is associated with the Y direction oscillation of stages ①, ② and ③, it should be theoretically unobservable in the frequency response measurement of stage ① in the X direction.
2. Modes III and IV are the two closely spaced modes associated with the oscillations of two main secondary stages (stages ② and ③). Along with mode II, these are the modes of interest in this paper.
3. Mode V is an out-of-plane mode in the Z direction due to the

Table 1
Modal analysis results for experimental setup designs of Fig. 2. Modal frequency reported in Hz.

Mode Order	Freq.	Description	Freq.	Description	Freq.	Description	Freq.	Description
I	15.2	"Rigid-body"	10.6	"Rigid-body"	14.8	"Rigid-body"	25.2	Y-mode
II	35.5	Y-mode[a]	29.7	Y-mode	29.7	Y-mode	33.1	"Rigid-body"
III	43.8	In-plane	44.9	Out-of-plane	83.0	CSM1	79.6	CSM1
IV	46.5	In-plane	51.5	Out-of-plane	91.3	CSM2	85.6	CSM2
V	54.1	In-plane	82.3	CSM1	123.8	Out-of-plane	235.1	Out-of-plane
VI	57.0	Out-of-plane	91.3	CSM2	128.0	Out-of-plane	237.8	In-plane
VII	67.0	Out-of-plane	111.2	In-plane	143.6	In-plane	272.8	In-plane
VIII	103.4	CSM1[b]	112.3	In-plane	144.2	In-plane	281.4	Out-of-plane
IX	116.1	CSM2[b]	149.6	In-plane	144.8	In-plane	282.0	In-plane
X	187.5	Out-of-plane	159.1	Out-of-plane	145.6	In-plane	283.6	In-plane
SEP_l	5.2		6.2		19.3		19.8	
SEP_h	5.8		2.6		4.2		24.5	

Notes: The terminology (i.e., "Rigid-body" mode, Y-mode, CSM1, and CSM2) is defined in *Section 1*. Shaded boxes refer to the extraneous modes.

Table 2
Physical parameters of final Fig. 2d (Improved) design.

Name	Symbol	Value	Unit
Plate height	H	25.4	mm
Main DPFM beam length	L_1	47.5	mm
Main DPFM beam thickness	T_1	0.625	mm
Minor DPFM beam length	L_2	47.5	mm
Minor DPFM beam thickness	T_2	1	mm
Span of the inner parallelogram, minor DPFM	L_3	40	mm
Intermediate stage dimension	L_4	85	mm
Distance between motor coil's center of gravity and the minor DPFM's rotational axis	L_5	30	mm
Minor DPFM's secondary stage dimensions	L_6	3	mm
	L_7	80	mm
Motion stage ①mass	m_1	0.4	kg
Secondary stages ② and ③ mass	m_2, m_3	0.06	kg
Intermediate stages ④ and ⑤ mass	m_4, m_5	0.177	kg

increase in the mass of stage ①. Mode VI is an in-plane rotational mode about the Z-axis due to the bending compliance of the secondary stages of the minor DPFMs. However, since modes V and VI appear at frequencies around 235 Hz (almost 3 times higher than mode IV), their contribution at the low frequencies is minor as desired.

4. The four closely spaced modes associated with the X direction oscillation of the four minor secondary stages appear at around 280 Hz. One of these is mode VII, shown in Fig. 5. Compared to the initial Fig. 2d design, these modal frequencies were increased by a factor of two.
5. Mode VIII of Fig. 2d (Improved) design is the same as mode V of the initial Fig. 2d design. The frequency of this mode increased from 123.8 Hz to 281.4 Hz. Additionally, mode VI mode of the Fig. 2ddesign, is now mode XIII of Fig. 2d (Improved) design (not shown in Fig. 5).

In summary, in Fig. 2d (Improved) design, there is a satisfactory separation between the CSM modes of interest (i.e., modes III and IV) and other modes, indicated by the high value of the separation indices: $SEP_l = 19.8$ and $SEP_h = 24.5$. Therefore, Fig. 2d (Improved) design was employed in the fabrication of the final experimental setup. Based on this design process, the relevant system parameters are summarized in the following table.

4. Experimental setup: hardware design

4.1. Hardware fabrication and assembly

Using the flexure mechanism geometry of Fig. 2d (Improved) design, the experimental setup hardware was fabricated and assembled for testing, as shown in Fig. 6. The flexure mechanism along with the reference ground frame were made monolithically from a 25.4-mm thick AL6061-T651 plate using wire-electric discharge machining (EDM), which offers a manufacturing tolerance of ± 0.005 mm. The other components of the assembly were fabricated by traditional machining, including an adapter between the actuator mover and stage ④, the balance mass attached stage ⑤ via another identical adapter, a bridge connected to the ground frame to mount the capacitance probe, and a flat target block for the capacitance probe connected to stage ①. Four screws (and associated stands) were used to connect the ground frame to the breadboard of an isolation table (Newport RS1000).

Tapped holes on the two secondary stages (stages ② and ③) were used to attach small masses. The intended mass asymmetry between stages ② and ③was achieved by adding masses with an incremental value of 0.5 g, which is 0.8% of the nominal mass of the secondary stages ($m_2 = m_3 = 60$ g).

4.2. X direction actuation and sensing

The primary goal of this experimental setup is to measure X direction frequency response at different Y direction operating points (Y_{1o}) for different levels of mass asymmetry (Δm_{23}). While the range of motion in the Y direction is large (to achieve a ± 10% of L_1 variation in the operating point), the range of motion for X direction can be small, which makes the selection of actuator and sensor in this direction easy. Using the beam dimensions of the minor DPFM, Aluminum as the material, and a safety factor of two against yielding, we set the range of motion in X direction as ± 1 mm. A mechanical stop was incorporated within the ground frame to prevent going over this X direction displacement range.

Based on the stiffness expression for DPFM [4,14] and the dimensions in Table 2, the stiffness of the experimental setup in the X direction can be computed to be 65.4 N/mm. However, the experiment did not require the flexure mechanism to be held at a non-zero displacement in the X direction. Instead, the frequency response system identification was conducted by sending a chirp sinusoid signal with zero mean, corresponding to a nominally zero X position of stage ①. For our experimental setup design, we selected a voice coil actuator from BEI Kimco Magnetics (Model: LA24-20-000A, force constant: 11.12 N/A, stroke: ± 8.26 mm, peak force 111 N, continuous force: 26 N) for the X direction actuation. This non-contact actuator is free of friction and backlash and provided adequate force and stroke for the frequency response measurements. An adapter was designed to provide connection between stage ④ and the mover of the actuator. The stator of the actuator was directly mounted on the ground frame via two X-direction screws. Shims were used to set the radial gap to be 0.38 mm (or. 0.015”,

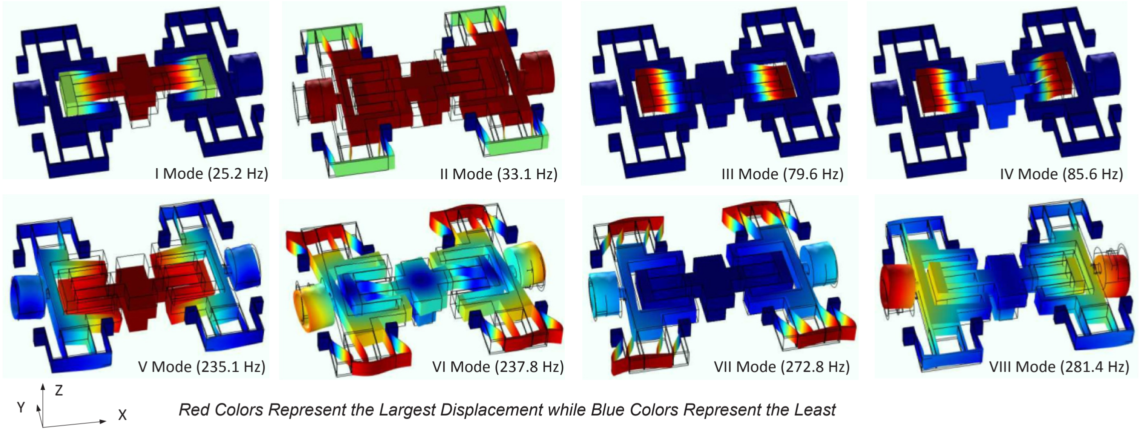

Fig. 5. Mode shapes of Fig. 2d (Improved) design.

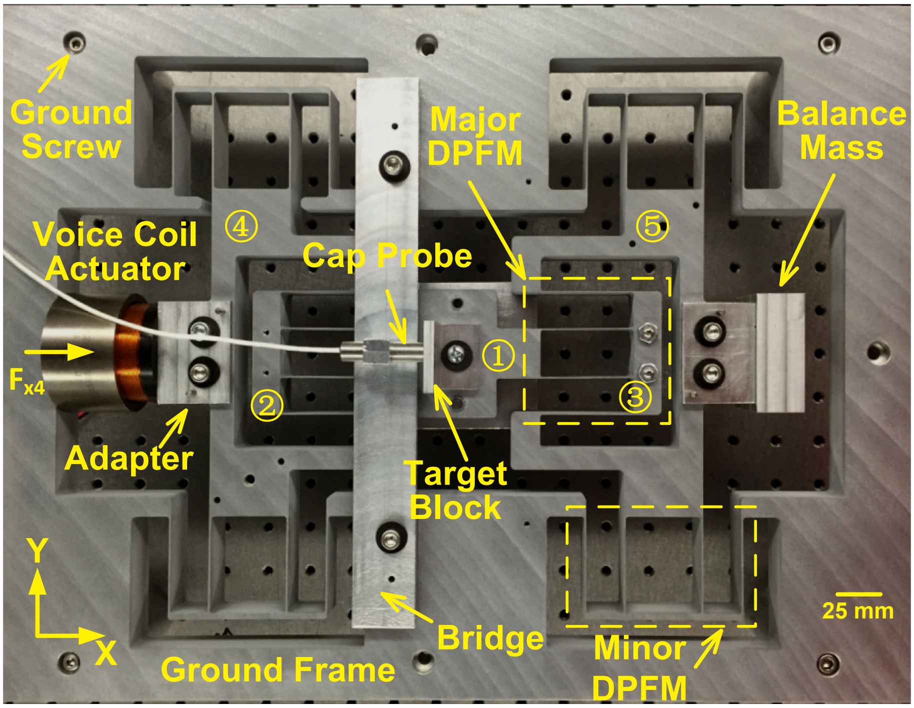

Fig. 6. Experimental setup.

per the data-sheet) between the stator and the mover of the actuator while tightening these screws. These shims were removed after the assembly.

A custom-built linear current amplifier based on the power op-amp MP111 was used to drive the actuator in a current mode at a bandwidth of 1 kHz [4]. This bandwidth of the current mode is sufficiently high to avoid any impact on the dynamics of interest, which is within 100 Hz.

For sensing the X displacement of stage ①, a non-contact sensor is desirable to avoid friction and backlash. Moreover, stage ① has displacements in both the X and Y directions; therefore, the X direction sensor should be able to accommodate large displacements in the Y direction. The desired range of X direction measurement is less than ± 1 mm, as discussed above. Capacitance probes meet all these requirements. Accordingly, a capacitance probe from Lion Precision (Model: C23C, Driver: CPL290, Range: 2 mm; RMS resolution: 40 nm) was chosen to measure the X direction displacement of stage ① w.r.t. the ground frame. An elevated bridge that clears all the moving stages was connected the ground frame via two screws. This bridge was used to mount the capacitance probe in the X direction.

The overall sensing and actuation system was operated using DSpace 1103 control system at a loop-rate of 5 kHz. The sensor sampling rate is the same as the loop-rate of the control system, resulting in a Nyquist frequency of 2500 Hz, which is sufficient for the estimation of the frequency response below 500 Hz (including the extraneous modes shown as Table 1).

4.3. Y direction actuation: virtual pulley

For the XY mechanism shown in Fig. 1, the operating point is set by applying a static Y direction force F_{1o}. One of the challenges in applying such a constant force on stage ① is that its position varies along both the X and Y directions. During the frequency response measurement, stage ① vibrates in the X direction with a small amplitude (~100 μm) in response to an X direction excitation at stage ④. Additionally, due to cross-axis coupling, there can be an even smaller but finite Y direction vibration at stage ①in response to an X direction excitation [2]. The Y direction actuation system has to accommodate these X and Y direction displacements during an X direction frequency response measurement. Furthermore, since this measurement has to be repeated at various Y direction operating points with a range of ± 5 mm, the Y direction actuation system has to be capable of providing the necessary force (F_{1o}) over this range and hold it constant at a given operating point. Finally, the Y actuation system should not impose any geometric constraints on stage ① that can change the system dynamics.

A potential option is to employ a non-contact force actuator such as a voice coil actuator or a moving magnetic actuator [31]. Apart from cost consideration, there are several practical challenges with this option. First, to provide desirable Y direction displacement (i.e. operating point), one needs to employ either closed loop position control in this direction or drive the actuator in current mode with a careful calibration of current to force and force to displacement characteristics. Second, these actuators are generally limited to a single axis (the actuation axis Y in this case), and do not allow off-axis X axis motions. Furthermore, the mover of these actuators would have to be attached to stage ①. But the added mass of this mover can negatively impact the dynamics of the entire experimental setup.

To overcome all these challenges, we chose a relatively simpler passive actuation method that utilizes an arrangement of cables to change the direction of vertical force provided by hanging weights to horizontal (i.e., Y direction) force on the motion stage. This arrangement is referred to as a “virtual pulley” [14,32] and is different from a traditional pulley, which also changes direction of force but introduces uncertainty in the horizontal actuation force due to rolling and/or sliding friction.

Fig. 7 shows a schematic of the virtual pulley employed in our experimental setup for Y direction actuation. The arrangement comprising three cable segments: a long nominally horizontal segment, a vertical segment, and a diagonal segment. All three segments are connected at a common point. The other end of the horizontal segment is attached the motion stage; the other end of the vertical segment is connected to a hanging weight; and the other end of the diagonal segment is connected to a rigid extension of the ground frame via the isolation table. This cable arrangement converts the vertical force of the weight W to a horizontal force F_{1o} on the motion stage in the Y direction. These two forces are simply related by the trigonometry of the cable arrangement [32] as stated below.

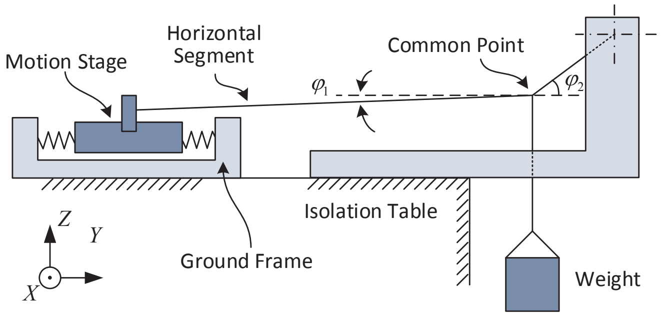

Fig. 7. Virtual pulley used for Y direction actuation.

$$F_{1o} = W(\cos\varphi_1 \cdot \tan\varphi_2 - \sin\varphi_1) \tag{4}$$

In this manner, a constant Y direction force F_{1o} (and resulting displacement Y_{1o}) is achieved by a known hanging weight, without the need for any active force control. The horizontal section of the cable was selected to be long enough (about 965 mm) so that it can absorb small X direction displacements of stage 1 without impacting the F_{1o} force. Any small Y direction vibration of the motion stage is also easily accommodated by the virtual pulley. The Y direction operating point is varied simply by changing the weight W and keeping track of any change in the cable arrangement trigonometry. The relevant angles are measured by taking a picture of the YZ plane. For small displacements, the virtual pulley provides the functionality of a frictionless pulley because it eliminates any rolling or sliding interfaces and any associated uncertainties.

For a given W, F_{1o} is obtained from the above equation, and the resulting Y_{1o} is calculated based on the Y direction stiffness k_y [4,14].

$$Y_{1o} = F_{1o}/2k_y$$

where

$$k_y = ET_1^3H/L_1^3 = 3992\ (N\cdot m^{-1})$$

The limitation of this actuation scheme is that the Y_{1o} operating point in the experimental setup is a derived quantity instead of an explicit position sensor such as linear encoder. Since we used calibrated weights, the accuracy of the derived operating point Y_{1o} is largely determined by the error in measuring the relevant angles and the error in estimating stiffness k_y. To quantitatively analyze the effect of angle measurement error, one can take a partial derivation of Eq. (4), while assuming that the maximum error of each angle measurement is the same (denoted as $\Delta\varphi$).

$$|dF_{1o}| \le |\frac{\partial F_{1o}}{\partial\varphi_1}\cdot d\varphi_1| + |\frac{\partial F_{1o}}{\partial\varphi_2}\cdot d\varphi_2| \le (|\frac{\partial F_{1o}}{\partial\varphi_1}| + |\frac{\partial F_{1o}}{\partial\varphi_1}|)\cdot\Delta\varphi \tag{5}$$

where

$$\frac{\partial F_{1o}}{\partial\varphi_1} = W\frac{\sin\varphi_1\cdot\tan\varphi_2 + \cos\varphi_1}{(\cos\varphi_1\cdot\tan\varphi_2 - \sin\varphi_1)^2};\ \frac{\partial F_{1o}}{\partial\varphi_2} = W\frac{-1}{(\cos\varphi_2)^2(\cos\varphi_1\cdot\tan\varphi_2 - \sin\varphi_1)^2} \tag{6}$$

Angles ($\varphi_1 = 1^\circ$, $\varphi_2 = 64^\circ$) were measured from a digital image of side (YZ plane) view of the setup. With a maximum error of angle measurement less than 0.5° (i.e., $|\Delta\varphi| \le 0.5^\circ$), one can derive $|dF_{1o}|/F_{1o} \le 2.49\%$. Similarly, one can derive the error in estimating stiffness k_y:

$$|dk_y| \le |\frac{\partial k_y}{\partial T_1}\cdot dT_1| + |\frac{\partial k_y}{\partial H}\cdot dH| + |\frac{\partial k_y}{\partial L_1}\cdot dL_1| \tag{7}$$

Assuming a manufacturing tolerance of ± 0.005 mm for all in-plane dimensions (wire-EDM) and plate thickness tolerance of 0.025 mm (accuracy and resolution of calipers used for direct measurement), assuming an exact value of elastic modulus ($E = 69$ GPa) and given the dimensions of our experimental setup (see Table 2), one can derive $|dk_y|/k_y \le 3.36\%$.

Substituting the relevant values, one can obtain $|dY_{1o}|/Y_{1o} \le 5.85\%$. We deemed this level of error in estimating Y_{1o} to be acceptable, because this error is static for the entire experiment (i.e., the angles and dimensions are invariant for a given setup). The impact of the error on experimental validation of model prediction is simply a scaling factor associated with the vertical axis on the CNMP zero map of Fig. 9. Such a scaling effect does not change the two main properties of the map: (1) the directional behavior when varying the operating point (i.e., CNMP zeros are observed only when $\Delta m_{23} > 0$); and (2) the shape of the CNMP zero region (i.e., CNMP zeros are observed when Y_{1o} is larger than a certain Δm_{23} dependent value).

If the cable were infinitely stiff then the mass of the hanging weight would contribute to the Y direction inertia of the motion stage, thereby impacting the modal frequencies and shapes designed in Section 3. But we intentionally used a long cable (horizontal and vertical segments) with a small cross-section (l x 7 strand construction, 0.012 in diameter) made of 302SS, which resulted in a finite cable stiffness. This leads to an additional low-frequency mode in the Y direction that serves to filter out the impact of the hanging weight on the Y direction inertia of the motion stage at the CSM frequencies of interest (~80–85 Hz). This Y-direction mode is unobservable in the X-direction transfer function.

5. Experimental results and discussion

To conduct the experiment, the frequency response from the X direction actuation force F_{x4} on stage ④to the X direction displacement (X_1) of the motion stage (see Fig. 1) was examined. The system identification was conducted in an open loop architecture. A 0.05 N chirp sinusoid signal with frequency content from 0.1 Hz to 500 Hz was used as the X actuator input force stage ④. Compared to white noise signal, a chirp signal leads to lower uncertainty error in the estimation of the frequency response because it is more concentrated in the selected frequency range. The time-domain response of X direction displacement was collected. The frequency response was then obtained by comparing the frequency spectrum of the input and output signals, using MATLAB spectrum analysis with frequency-dependent resolution.

A comparison between model prediction and experimental result is presented in Fig. 8, for a representative operating condition where mass asymmetry (Δm_{23}) is +10% and operating point (Y_{1o}) is 8% of L_1. The damping ratios for the model were estimated from the experimental results based on Rayleigh damping [33]. These estimated damping ratios were 0.009 for the "rigid-body" mode (mode II, Table 1) and 0.004 for the closely spaced modes (modes III and IV, Table 1). The "rigid-body" mode has a larger damping ratio since it is associated with the oscillation of the entire flexure mechanism, which leads to a larger amount of area exposed to the viscous air environment. The back electromagnetic force (back EMF) of the voice coil actuator does not contribute to the damping ratio of the "rigid-body" mode when the drive amplifier operates in the current control mode.

Key observations from the experimental measurement are as follows. First, the first three modes (Y mode or Mode I is almost unobservable) in the experimental results match well with the dynamic model of the XY flexure mechanism. Furthermore, the change in the frequencies of the CSM (modes III and IV) due to variation of the operating point agrees with the model prediction (not shown in Fig. 8). Second, the CSM (modes III and IV) are shown to be well-separated from other modes, as expected from the experimental setup design (Section 2). The first high order extraneous mode occurs at 210 Hz, with a separation index of $SEP_h = 20.5$, (experimental result matches FEA model). Moreover, it can be seen from Fig. 8 that, the higher order extraneous modes have a minor contribution on the dynamics of interest at low frequency region as desired. Third, and most importantly, CMP-CNMP zeros are observed exactly as predicted by the theoretical model. In Fig. 8b, the 360° phase drop due to the existence of CMP-

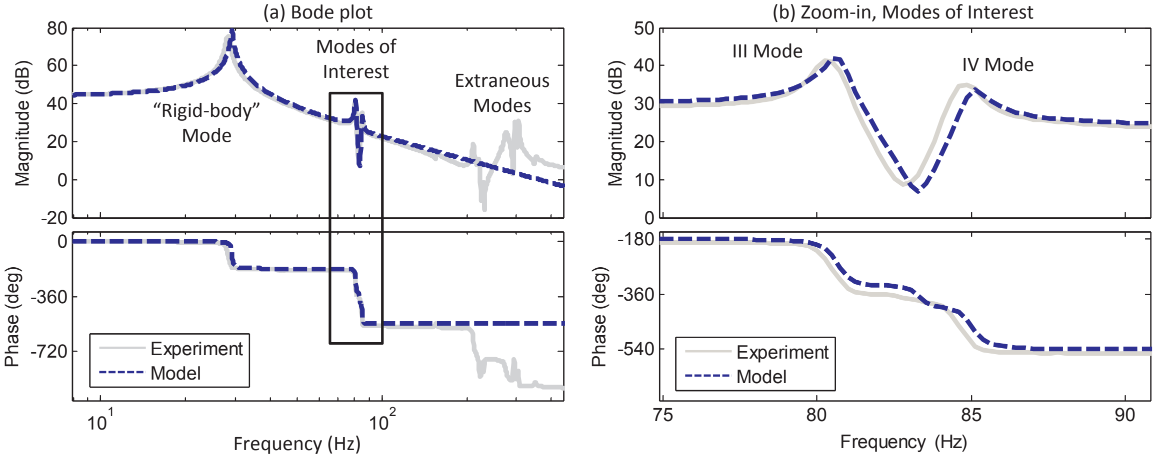

Fig. 8. Frequency response ($\Delta m_{23} = 10\%$, $Y_{1o} = 8\%$ of L_1): (a) over 500 Hz frequency range (b) zoom-in on the closely space modes (III and IV).

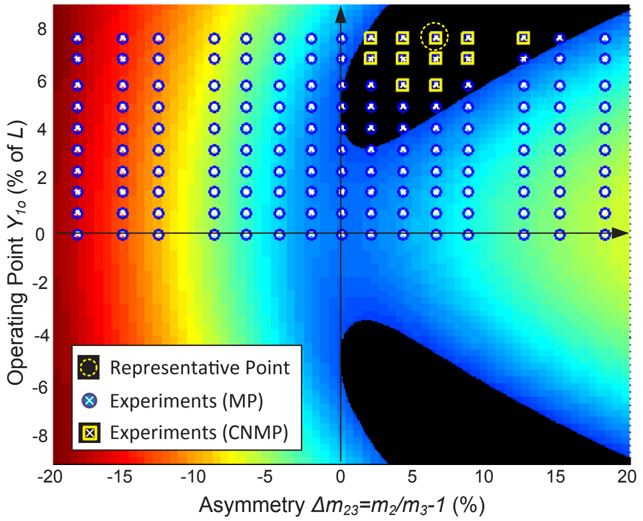

Fig. 9. Complex non-minimum phase zeros map: simulation and experimental results. The frequency response at the representative point is shown in Fig. 8.

CNMP zeros is very clearly seen.

Results from multiple experimental measurements, one for each combination of operating point (Y_{1o} normalized w.r.t. beam length L_1) and parametric mass asymmetry (Δm_{23}), were overlaid with the model predictions [2] on a zero map (Fig. 9). The model predicts that CNMP zeros should arise in the black regions of this zero map. Experimental measurements were conducted over a two-variable grid spanning 150 operating conditions (10 values of Y_{1o} and 15 values of Δm_{23}). Note that only half of the area was tested due to the symmetric properties of the flexure mechanism and the CNMP zero map w.r.t. positive/negative Y operating points. The squares indicate the conditions when the CMP-CNMP zeros are present in the experimental frequency response. In contrast, the solid circles indicate conditions when CMP-CNMP zeros are absent, and instead the zeros are minimum phase. Lastly, the dashed circle represents the specific operating condition presented in Fig. 8.

Fig. 9 shows that the experimental results match well with the model prediction. It is experimentally confirmed that for the situation of negative asymmetry ($\Delta m_{23} < 0$), the entire operating range is free of CMP-CNMP zeros, as expected from the model. This is an important experimental validation since the model prediction was non-obvious. For $\Delta m_{23} > 0$, experimental findings largely agree with model prediction of the CMP-CNMP zero region and confirm that CMP-CNMP zeros appear only when the Y_{1o} operating point is larger than a certain value. Third, when the situation is nominally symmetric ($\Delta m_{23} \approx 0$), the existence of CMP-CNMP zeros is sensitive to positive mass parameter variation at large operating points ($Y_{1o} \approx$ 6–8%).

The slight mismatch between the experimental and predicted CMP-CNMP regions in Fig. 9 can be attributed to the following factors.

1. The CNMP map compiled from the theoretical model was based on the assumption of neglecting the damping [2]. However, as shown in previous work [1], the presence of damping shifts the predicted CMP-CNMP zero quartet to the left side of the complex plane and the onset of CNMP zeros happens at larger operating points. In other words, the presence of finite damping "delays" the system's transition from two pairs of minimum phase zeros to the CMP-CNMP zero quartet. For example, in Fig. 9, for the operating point $Y_{1o} = 4\%$ and $\Delta m_{23} = 2\%$, the model predicted CMP-CNMP zeros are not observed in the experiments.
2. The second factor that impacts the experimental results is the indirect estimation of the operating point Y_{1o}, which can have an error of 5.85% as shown in Section 3.3. As noted before, this is scaling error in the vertical axis of the CNMP map. While this error does not change the fundamental attributes of the CNMP zero map, it can produce the slight discrepancy seen between model-based predictions and experimental measurements in Fig. 9. In hind-sight, to reduce the estimation error in Y_{1o}, a linear encoder could have been used to explicitly measure the Y direction displacement of stage① with respect to the ground frame.

6. Conclusions

We presented an experimental confirmation of the existence of CNMP zeros, predicted by a previous theoretical model [1,2], under specific conditions (operating point and parametric asymmetry) in a certain XY flexure mechanism. This XY flexure mechanism exhibits a low frequency rigid body mode and a pair of closely spaced modes at higher frequency. This experimental validation is significant in that it corroborates the various assumptions made in previous modeling of the system dynamics. These assumptions include the importance of beam arc-length conservation and the resulting non-linear coupling between the X and Y direction displacements. The experiments also confirm that this coupling varies slightly with the operating point and parametric asymmetry, resulting in small changes in the modal residues (magnitude and signs) of the closely spaced modes. These changes are shown to give rise to a CMP-CNMP zero quartet, as predicted by the theoretical model.

From a mechatronic design stand-point, this experimental validation provides a better understanding of the system dynamics (specifically CNMP zeros), which in turn can inform physical system design decisions in a deterministic manner. We demonstrate that independent of any other design considerations (e.g. collocation of sensor and actuator, slaving of secondary stages in DPFM, additional damping, etc.) CNMP zeros can be eliminated via an intentional use of parametric asymmetry. This simple yet non-obvious physical system design decision can lead to better control system design and performance of a flexure-based motion stage.

Even though the CNMP zeros experimentally investigated here arise due to the closely spaces modes associated with the Y displacement of the secondary stages of the two DPFM, such zeros can more generally arise from any two closely spaced modes in a flexure mechanism. The experimental hardware setup design and measurement methods presented in this paper are equally relevant and applicable to any such scenario.

This work also reveals several questions that currently under investigation. For example, the fact that negative mass asymmetry eliminates CNMP zeros while positive asymmetry does not (Fig. 9) is due to the location of actuator at stage ④ (Fig. 1). Had the actuator been located at stage ⑤, the zero map of Fig. 9 would be flipped about its vertical axis. Similarly, actuating at both stages ④ and ⑤ can potentially eliminate the CNMP zeros but remains to be proven mathematically. There remains a need for a more general modeling effort and resulting design guidelines that relate the physical topology of a flexure mechanism along with sensor(s) and actuator(s) locations to the existence of various types of zeros, including CNMP zeros.

Acknowledgement

This research was supported in part by a National Science Foundation grant (CMMI # 1634824).

References

[1] Cui L. Complex non-minimum phase zeros in the dynamics of flexure mechanisms. University of Michigan; 2017.
[2] Cui L, Okwudire C, Awtar S. Modeling complex nonminimum phase zeros in flexure mechanisms. J Dyn Syst Meas Control 2017;139:101001.
[3] Seugling RM, LeBrun T, Smith ST, Howard LP. A six-degree-of-freedom precision motion stage. Rev Sci Instrum 2002;73:2462–8.
[4] Awtar S, Parmar G. Design of a large range XY nanopositioning system. J Mech Robot 2013;5:021008.
[5] Åström KJ. Limitations on control system performance. Eur J Control 2000;6:2–20.
[6] Middleton RH. Trade-offs in linear control system design. Automatica 1991;27:281–92.
[7] Goodwin GC, Woodyatt A, Middleton RH, Shim J. Fundamental limitations due to jω-axis zeros in SISO systems. Automatica 1999;35:857–63.
[8] Freudenberg JS, Looze DP. Right half plane poles and zeros and design trade-offs in feedback systems. IEEE Trans Autom Control 1985;30:555–65.
[9] Levine WS. The control systems handbook: control system Advanced methods. CRC press; 2010.
[10] Miu DK. Physical interpretation of transfer function zeros for simple control systems with mechanical flexibilities. J Dyn Syst Meas Control 1991;113:419–24.
[11] Coelingh E, de Vries TJ, Koster R. Assessment of mechatronic system performance at an early design stage. Mechatron IEEE ASME Trans 2002;7:269–79.
[12] Lee YJ, Speyer JL. Zero locus of a beam with varying sensor and actuator locations. J Guid Control Dyn 1993;16:21–5.
[13] Martin GD. On the control of flexible mechanical systems. Standford University; 1978.
[14] Awtar S. Synthesis and analysis of parallel kinematic XY flexure mechanisms. MIT; 2003.
[15] Schneiders M, Van De Molengraft M, Steinbuch M. Benefits of over-actuation in motion systems. American control conference, 2004. Proceedings of the 2004: IEEE. 2004. p. 505–10.
[16] Balas MJ. Active control of flexible systems. J Optim Theory Appl 1978;25:415–36.
[17] Galvan SD, Heertjes M, Dunand R. Plant enhancements in motion systems by modal control. American control conference (ACC), 2012: IEEE. 2012. p. 5348–53.
[18] Brouwer DM, Otten A, Engelen J, Krijnen B, Soemers H. Long-range elastic guidance mechanisms for electrostatic comb-drive actuators. International Conference of the European Society for Precision Engineering and Nanotechnology (EUSPEN). May 2010. p. 41–50.
[19] Panas RM, Hopkins JB. Eliminating underconstraint in double parallelogram flexure mechanisms. J Mech Des 2015;137:092301.
[20] Olfatnia M, Sood S, Gorman JJ, Awtar S. Large stroke electrostatic comb-drive actuators enabled by a novel flexure mechanism. J Microelectromech Syst 2013;22:483–94.
[21] Olfatnia M, Cui L, Chopra P, Awtar S. Large range dual-axis micro-stage driven by electrostatic comb-drive actuators. J Micromech Microeng 2013;23:105008.
[22] Varanasi KK. Ibration damping using low-wave-speed media with applications to precision machines. Massachusetts Institute of Technology; 2004.
[23] Parmar G. Dynamics and control of flexure-based large range nanopositioning systems. 2014.
[24] Roy NK, Cullinan MA. Design and characterization of a two-axis, flexure-based nanopositioning stage with 50 mm travel and reduced higher order modes. Precis Eng 2018;53:236–47.
[25] Tohyama M, Lyon RH. Zeros of a transfer-function in a multi-degree-of-freedom vibrating system. J Acoust Soc Am 1989;86:1854–63.
[26] Loix N, Kozanek J, Foltete E. On the complex zeros of non-colocated systems. J Struct Control 1996;3:79–87.
[27] Awtar S, Craig KC. Electromagnetic coupling in a dc motor and tachometer assembly. J Dyn Syst Meas Control 2004;126:684–91.
[28] Acar C, Shkel A. MEMS vibratory gyroscopes: structural approaches to improve robustness. Springer Science & Business Media; 2008.
[29] Awtar S, Slocum A, Sevincer E. Characteristics of beam-based flexure modules. J Mech Des 2007;129:625–39.
[30] Wikipedia. Torsion constant.
[31] Hiemstra DB, Parmar G, Awtar S. Performance tradeoffs posed by moving magnet actuators in flexure-based nanopositioning. Mechatronics. IEEE ASME Trans 2014;19:201–12.
[32] Awtar S, Mariappan DD. Experimental measurement of the bearing characteristics of straight-line flexure mechanisms. Precis Eng 2017;49:1–14.
[33] Meirovitch L. Analytical methods in vibration vol. 19. New York, NY: The Mcmillan Company; 1967.